THE PHYSICAL CONDITIONS OF THE INTRINSIC N v NARROW ABSORPTION LINE SYSTEMS OF THREE QUASARS

Jian Wu[1], Jane C. Charlton[1], Toru Misawa[1,4], Michael Eracleous[1,2], and Rajib Ganguly[3]

[1] Department of Astronomy & Astrophysics, The Pennsylvania State University, 525 Davey Lab, University Park, PA 16802, USA; jwu@astro.psu.edu
[2] Center for Gravitational Wave Physics, The Pennsylvania State University, University Park, PA 16802, USA
[3] Department of Computer Science, Engineering, & Physics, University of Michigan-Flint, 213 Murchie Science Building, 303 Kearsley Street, Flint, MI 48502, USA

ABSTRACT

We employ detailed photoionization models to infer the physical conditions of intrinsic narrow absorption line systems found in high-resolution spectra of three quasars at $z = 2.6$–3.0. We focus on a family of intrinsic absorbers characterized by N v lines that are strong relative to the Lyα lines. The inferred physical conditions are similar for the three intrinsic N v absorbers, with metallicities greater than 10 times the solar value (assuming a solar abundance pattern), and with high ionization parameters ($\log U \sim 0$). Thus, we conclude that the unusual strength of the N v lines results from a combination of partial coverage, a high ionization state, and high metallicity. We consider whether dilution of the absorption lines by flux from the broad emission line region can lead us to overestimate the metallicities and we find that this is an unlikely possibility. The high abundances that we infer are not surprising in the context of scenarios in which metal enrichment takes place very early on in massive galaxies. We estimate that the mass outflow rate in the absorbing gas (which is likely to have a filamentary structure) is less than a few $M_\odot$ yr^{-1} under the most optimistic assumptions, although it may be embedded in a much hotter, more massive outflow.

Key words: quasars: absorption lines – quasars: individual (HE0130–4021, Q1009+2956, HS1700+6416)

Online-only material: color figures, extended figure

1. INTRODUCTION

Intrinsic absorption lines seen in the spectra of quasars are thought to originate in ionized gas physically related with the quasar "central engine" (e.g., Hamann et al. 2004). They include resonance lines that appear in the rest-frame UV band, such as N v, C iv and/or high-ionization species that have absorption lines and edges in the soft X-ray band, such as O vii and O viii (e.g., Reynolds 1997; Giustini et al. 2010). The intrinsic UV absorption lines are usually blueshifted relative to the quasar emission lines and they are believed to arise from gas that is outflowing from the immediate vicinity of the central engine. Lines that are blueshifted by less than 5000 km s^{-1} are conventionally regarded as *associated* absorption lines (AALs). Many of these may indeed be connected to broad emission line region (BELR; Ganguly et al. 2001) and to X-ray "warm" absorbers (Mathur et al. 1995; Brandt et al. 2000). These absorption lines thus trace the physical conditions and kinematics surrounding the central engine over a wide range of redshifts, and thus provide a diagnostic of quasar evolution.

Narrow intrinsic absorption lines (NALs) typically have widths ≲500 km s^{-1} so that their doublets can be separated at high spectral resolution (see Hamann & Sabra 2004). This is in contrast to broad absorption lines (BALs) whose width can reach 30,000 km s^{-1} (Trump et al. 2006). Intrinsic NALs studies are complementary to studies of BALs, since they probe different regions in the quasar surroundings. Although the intrinsic NALs are more difficult to identify, several practical considerations make the derivation of their physical conditions more straightforward than for BALs (Hamann & Ferland 1999). Because NALs are often unsaturated and resolved, we can measure directly the NAL coverage fractions and column

densities of various ions. In BAL systems, doublet transitions are often self-blended, making such measurement more difficult.

Approximately 60% of all quasars show evidence of outflows (Misawa et al. 2007; Ganguly & Brotherton 2008). Although statistical methods can be used to determine this, partial coverage of doublets and multiplets and time variability analysis are the two most commonly used ways to determine decisively if a particular NAL system is intrinsic. These signatures are only seen in low-ionization transitions of intervening absorbers, and only rarely in the case of small molecular clouds that could be smaller than the projected size of the background quasar BELR (e.g., Jones et al. 2010; Ivanchik et al. 2010). Partial coverage is described by the coverage fraction C_f, which is the fraction of photons from the background source that pass through the absorber (Barlow et al. 1997). It can be estimated using the residual flux ratio of resonance doublets (e.g., Barlow & Sargent 1997; Ganguly et al. 1999). Variability of the absorption lines could be caused by transverse motion of the absorbing material or by changes in its ionization state (Hamann 1997; Misawa et al. 2005). Using UV spectra of $z \leqslant 1.5$ quasars observed at two different epochs separated by 4–10 yr with the *Hubble Space Telescope*, Wise et al. (2004) concluded that a minimum of 21% of the AALs are variable. A similar conclusion was reached for $z \sim 2$ quasars by Narayanan et al. (2004).

Early work investigating metal abundances using narrow AALs indicated supersolar metallicities, i.e., $Z \geqslant Z_\odot$ (Petitjean et al. 1994; Tripp et al. 1996; Hamann 1997). More recent work measures metallicities consistent with the previously determined values, and in some cases, it has provided a more stringent constraint. Papovich et al. (2000) analyzed a $z = 1.207$ AAL system toward Q0122+0388 with the help of photoionization models and found $Z \sim 2 Z_\odot$. Fields et al. (2005) found that the metallicity must be at least $5 Z_\odot$ in order to produce the high-ionization absorption lines (O vi, C iv, and N v) of the narrow-line Seyfert galaxy Mrk 1044. Gabel et al.

(2006) also found supersolar abundances by modeling the AALs of the quasar J2233 − 606, with [C/H], [O/H] ≈ 0.5–0.9, and [N/H] ≈ 1.1–1.3. High metallicity, up to $3 Z_\odot$, is suggested in the study of quasar PG 0935+417 (Hamann et al. 2004). A study of the outflow from Mrk 279 by Arav et al. (2007) has found an overabundance carbon, nitrogen, and oxygen relative to the Sun by factors of 2.2 ± 0.7, 3.5 ± 1.1, and 1.6 ± 0.8, respectively. Moreover, photoionization modeling of associated NALs systems finds metallicities ranging between a few and 20 times the solar value (e.g., Petitjean et al. 1994; Tripp et al. 1996; D'Odorico et al. 2004). Such high metal abundances are also inferred from analysis of the broad emission lines. For example, Hamann et al. (2002) find that α-elements, such as C and O, are overabundant in the BELRs of quasars by a factor of ∼3 relative to the Sun.

Previous studies indicate that the AALs and BALs are located within the scale of the host galaxy and suggest that the absorbers are physically associated with and may originate from the quasar outflow. For example, the strengths of the excited-state Si II* AALs in the high-resolution spectrum of 3C 191 indicate a distance of 28 kpc from the quasar assuming the gas is photonionized (Hamann et al. 2001). By studying the metastable excited levels of Si II and Si II*, Dunn et al. (2010) determine the distance to the outflow for attenuated and unattenuated spectral energy distributions (SEDs) of ∼6 kpc or ∼17 kpc, respectively. Variability analysis of a C IV NAL complex towards quasar HS1603 +3820 constrains an upper limit on the distance of $r \leqslant 6$ kpc from the continuum source (Misawa et al. 2005).

Although it is generally agreed upon that intrinsic absorption lines are formed in an outflow from the central engine, there is no consensus on the geometry or the driving force of such an outflow. In the model of Murray et al. (1995), which was developed further by Proga et al. (2000), the wind is launched from the entire surface of the accretion disk, with many denser, absorbing filaments distributed throughout. In this picture, the BALs appear at low latitudes (small angles from the plane of the disk) when the line of sight passes directly through the dense, high velocity wind. The NALs could form at higher latitudes when the line of sight intercepts a dense filament in the hot, low-density flow. Elvis (2000), instead, proposed a funnel-shaped thin shell outflow model, in which the wind rises vertically from a narrow range of radii on a disk in the BELR. The high-ionization UV NALs and the X-ray "warm absorbers" are seen when the disk is viewed at a low latitude, through the wind. When viewed along the fast outflow, the full range of velocity is seen in absorption with a large total column density, giving rise to a BAL. Recent work indicates that the column densities measured in the X-ray spectra of quasars hosting intrinsic NALs are considerably lower than what the Elvis (2000) scenario posits (Misawa et al. 2008; Chartas et al. 2009), which suggests a preference on the model of Murray et al. (1995). There is also a suggestion that in some objects, the outflows are directed in the polar direction, parallel to the axis of the accretion disk (see, for example, Ghosh & Punsly 2007; Zhou et al. 2006; Brotherton et al. 2006). In the context of such a picture, and by analogy with equatorial wind models, the absorbers giving rise to NALs could be detached from the dense part of the outflow and become visible along different lines of sight. Previous studies have shown that the absorbing clumps originate at similar physical locations and are driven by radiative acceleration. This is supported by the explanation of a double trough in the C IV BAL by the "line-locking" effect (e.g., Arav et al. 1995). A striking case can be seen in Srianand et al. (2002), which reports an observation of a highly structured flow in which distinct components have similar velocity separations.

Misawa et al. (2007) identified two families of intrinsic absorption lines among 39 intrinsic NAL systems. The "strong-N V" family is characterized by strong, partially covered N V, relatively weak Lyα (less than twice the equivalent width of N V), occasionally detected C IV, and O VI lines (sometimes even stronger than the N V lines). The "strong-C IV" family, on the other hand, is characterized by strong, partially covered C IV doublets, strong, usually black Lyα lines, and relatively weak or undetected N V. A possible third family, characterized by strong O VI lines is discussed by R. Ganguly et al. (2010, in preparation). They primarily used partial covering to diagnose the intrinsic nature of the systems, i.e., they found that the members of the doublet could not be fit simultaneously assuming full coverage. Depending on the geometries and locations of the continuum source and BELRs (and empirically on their positions relative to the emission lines), the absorber can partially cover either or both (Ganguly et al. 1999). There may be overlap between the C IV and O VI categories as some absorption systems can possess both strong-C IV and O VI lines. Further observations covering both of these lines are needed to investigate this issue. These different types of NALs are of interest because they may allow us to probe different regions of the outflow. These three families of NALs may represent different lines of sight through the outflow, which is also suggested by the relations between the properties of UV NALs and the X-ray properties of the quasars that display them (e.g., Chartas et al. 2009).

The question we address in this paper is the origin of the intrinsic N V NALs. To this end, we construct photoionization models for the strong-N V absorption systems in the spectra of three radio-quiet quasars from the HIRES/Keck sample studied by Misawa et al. (2007). This sample contains 37 optically bright quasars at $z = 2$–4. We choose these particular three quasars because their spectra exhibit characteristics of the "strong-N V" family. In addition, these three systems offer many observational constraints because many ions are covered in their spectra, and the N V absorption lines have *relatively* simple profiles. Similar systems, containing multiple absorption components spread over thousands of km s^{-1} have been reported in the spectra of RX J1230.8 + 0115 (Ganguly et al. 2003) and 3C 351 (Yuan et al. 2002).

In Section 2, we describe the absorption profiles of the three intrinsic N V NAL systems. In Section 3, we introduce our method for modeling the three systems using the Cloudy photoionization code (Ferland 2006). The modeling results, in the form of constraints on metallicity, ionization parameter, and volume number density are presented in Section 4. In Section 6, we discuss possible interpretations of our results on the location of the absorbers in the quasar winds. We present a summary and conclusion in Section 7. The cosmology we use in this paper is $\Omega_\Lambda = 0.7$, $\Omega_M = 0.3$, and $h = 0.7$, which leads to the luminosity distances listed in Table 1.

2. DATA

The Keck/HIRES spectra of our three intrinsic N V systems are described in Misawa et al. (2007). The spectral resolution is $R = 37,500$, or ∼7 km s^{-1}. Table 1 summarizes the basic properties of the three absorption systems and of the quasars that host them. The transitions listed are detected at a 5σ confidence level at the NAL redshift. The sign of the velocity of a system

Table 1
Summary of Properties of Intrinsic NAL Systems[a]

Quasar	z_{em}	d_L[b] (Gpc)	$\log L_{bol}$[c]	$\log Q_i$[d]	z_{abs}[e]	v_{ej}[f] (km s^{-1})	Spectral Coverage[g] (Å)	Transitions Detected
HE0130−4021	3.030	25.7	48.36	58.40	2.9739	4204	3612–6084	Lyα, Lyβ, C III, N V, O VI
Q1009+2956	2.644	21.8	48.49	58.53	2.6495	−453	3093–4623	Lyα, Lyβ, C III, S VI, N V, O VI
HS1700+6416	2.722	22.6	48.98	58.97	2.7125	764	3726–6190	Lyα, Lyβ, C IV, N V, O VI

Notes.
[a] Adopted from Misawa et al. (2007).
[b] The luminosity distance, assuming $\Omega_\Lambda = 0.7$, $\Omega_M = 0.3$, and $h = 0.7$.
[c] The log of the bolometric luminosity (in erg s^{-1}). See details in Section 3.2 of the text.
[d] The log of the ionizing photon rate (in s^{-1}). See details in Section 3.2 of the text.
[e] Absorption system redshift determined by finding the wavelength that divides the optical depth of the N V λ1239 line in half.
[f] Ejection velocity relative to emission lines. A positive sign denotes a blueshift.
[g] Wavelength range covered by the Keck spectrum.

Table 2
Results of Decomposition of N V Doublet Profiles[a]

Quasar	Kinematic Component	v_{ej}[b] (km s^{-1})	v_{rel}[c] (km s^{-1})	$\log N_{NV}/cm^{-2}$ [d]	b[e] (km s^{-1})	C_f[f]
HE0130−4021	1	4324	−120	14.18 ± 0.04	16.6 ± 0.9	0.43 ± 0.03
	2	4275	−71	14.2 ± 0.1	20 ± 8	0.16 ± 0.04
	3	4236	−32	13.9 ± 0.1	13 ± 2	0.49 ± 0.08
	4	4209	−5	14.8 ± 0.3	32 ± 5	0.13 ± 0.03
	5	4084	+121	15.9 ± 0.5	28 ± 5	0.10 ± 0.02
	6	4020	+184	15.0 ± 0.3	17 ± 2	0.13 ± 0.03
	7	3891	+313	15.2 ± 0.6	6 ± 1	0.37 ± 0.02
	8	3952	+252	14.62 ± 0.06	34 ± 3	0.21 ± 0.02
	9	4210	−6	13.51 ± 0.01	12.6 ± 0.3	1.00[g]
Q1009+2956	1	−453	−5	13.70 ± 0.29	14.3 ± 1.7	0.62 ± 0.11
	2	−455	+2	14.79 ± 1.48	3.40 ± 1.90	0.70 ± 0.06
	3	−461	+7	14.63 ± 0.28	13.0 ± 2.1	0.22 ± 0.05
HS1700+6416	1	771	−9	14.18 ± 0.05	11.0 ± 0.5	0.43 ± 0.02
	2	766	+2	14.62 ± 0.04	25.6 ± 0.5	0.33 ± 0.02
	3	450	+314	13.8 ± 0.1	18.4 ± 0.8	$0.36^{+0.07}_{-0.06}$

Notes.
[a] The errors are a combination of the continuum fitting errors and Voigt profile fitting errors.
[b] Ejection velocity relative to the emission lines. A positive sign denotes a blueshift.
[c] Velocity offset relative to the redshift of the entire absorption line complex. The sign of the velocity is set to be positive, if the lines are redshifted from the system center.
[d] The N V column density inferred from the Voigt profile fit.
[e] Doppler parameter.
[f] Effective coverage fraction.
[g] There is no error bar for this entry because our fitting yields $C_f > 1$, which is unphysical. Thus, we set $C_f = 1.00$ when we fit this component.

is taken to be positive, if the line is blueshifted, i.e., if the gas appears to be outflowing relative to the quasar; this is the opposite convention from that adopted in Misawa et al. (2007). In the same table, we also list the 4400 Å flux densities (taken from Misawa et al. 2007), as well as the bolometric luminosities and ionizing photon rates (obtained as described in Section 3).

Figures 1–3 present, for each system, absorption profiles for transitions which are used as modeling constraints. An example of the best models we have found (discussed in later sections) is also shown in each figure. The velocity of an entire system is defined by the optical depth-weighted center of the strongest member of the N V doublet. We describe each system below.

HE0130−4021 ($z_{abs} = 2.973915$; Figure 1). The system is found ∼4000 km s^{-1} blueward of the quasar emission redshift, just within the associated region. This system is kinematically more complex than the other two, with nine components in

each N V line, spreading over ∼500 km s^{-1}. All but one of these components have small coverage fractions ($C_f < 0.5$; see Table 2). The strong features in the Lyα panel of Figure 1 at ∼ − 280, 50, 110, and 210 km s^{-1} cannot be Lyα components because the corresponding Lyβ components are not detected. Thus only portions of the Lyα profile can be used as constraints, but it is clear that the absorption in Lyα is quite weak. The O VI doublet appears to be detected in many of the same components as N V, though inconsistencies between O VI λ1032 and O VI λ1038 betray a number of blends. For this system the alignment of kinematic components of different transitions is convincing and it seems at least some of the O VI absorption is real. We can use the observed absorption at the positions of O VI λλ1032, 1038 as an upper limit.

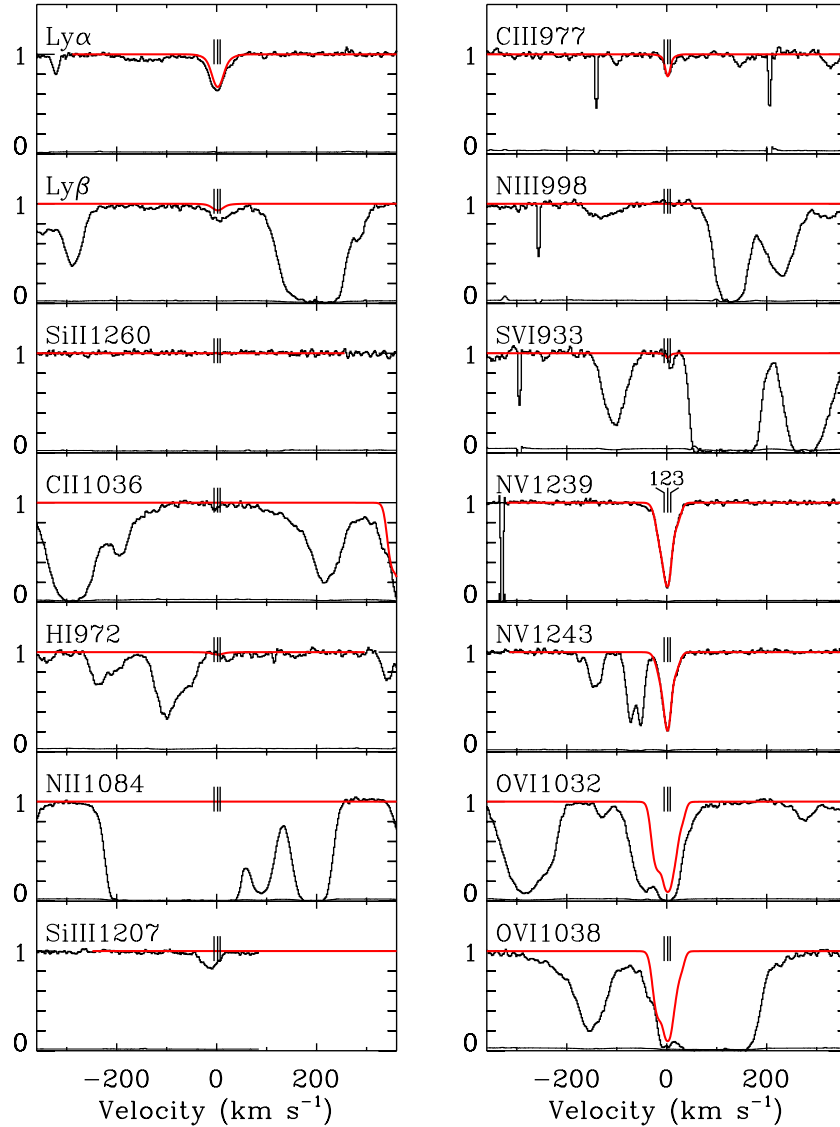*Q1009+2956 ($z_{abs} = 2.649510$; Figure 2).* This system is ∼450 km s^{-1} redward of the quasar emission redshift. The N V
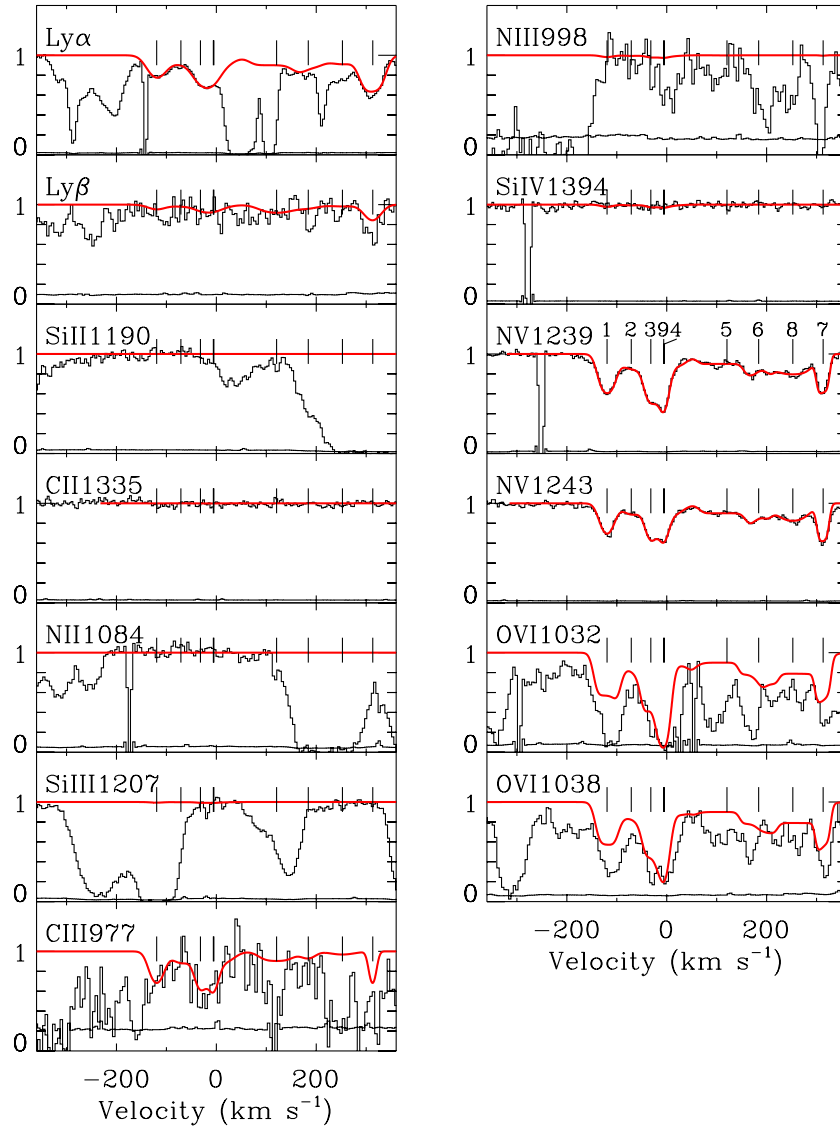
Figure 1. Plots of absorption lines from all the transitions used as constraints for the $v_{ej} = 4204$ km s^{-1} ($z_{abs} = 3.973915$) absorption system in the spectrum of HE0130−4021. Transitions are ordered by increasing ionization potential, except that Lyα and Lyβ (H I1026) are always the first. The zero point of the velocity scale is set by the bisector of the strongest blend of the N V line (the bisector divides the optical depth of the blend in half). Overplotted (red) in each panel is the best theoretical profile we obtained by adjusting the photoionization model parameters (see Section 4 for details). We mark each kinematic (Voigt) component using a tick mark; the component numbers are printed in the N V λ1239 panel. The corresponding components for different transitions have the same partial coverage factor (see Section 3). The corresponding components for different transitions have the same partial coverage factor (see Section 3), which are listed in Table 2.

(A color version of this figure is available in the online journal.)

$\lambda\lambda$1239, 1242 doublet of this system exhibits partial coverage in each of the three blended kinematic (Voigt) components required to fit its asymmetric profile, with the strongest component having $C_f = 0.70 \pm 0.06$ (Figure 2 and Table 2). Lyα and Lyβ are detected, but are unusually weak compared to N V. The ratio of Lyα to Lyβ is reasonable, but differences in the shapes of these lines, particularly the presence of a wing on the red side of the Lyβ profile, suggest a possible blend with another line. We will thus weight the Lyα line more heavily as a constraint. Narrow C III λ977 and S VI λ933 lines appear to be detected, albeit with some uncertainty because of their location in the Lyα forest. The red member of S VI $\lambda\lambda$933, 945 doublet is heavily blended and thus cannot be used to judge whether this doublet is truly detected or not. The feature at the position of Si III λ1207 is not aligned with the C III λ977 and N V λ1239 profiles and is too

broad, so we believe that we only have an upper limit on Si III λ1207 absorption from this system. There is absorption at the positions of both members of the O VI $\lambda\lambda$1032, 1038 doublet, however the minima are not aligned with each other or with the N V profile. The O VI λ1032 is too broad relative to O VI λ1038, and both transitions are clearly affected by blends. The limits on O VI for this system are not restrictive constraints for our models.

HS1700+6416 ($z_{abs} = 2.7125$; Figure 3). This system is $\sim$750 km s^{-1} blueward of the quasar emission redshift. The N V $\lambda\lambda$1239, 1242 and C IV $\lambda\lambda$1548, 1550 doublets are detected in this system, as well as Lyα and Lyβ (Figure 3). The same system was presented in Barlow et al. (1997), who found it to vary significantly on a timescale of $\sim$6.5 months in its rest frame. The central absorption is detected at $z \sim 2.7125$ ($v_{rel} \sim 0$ km s^{-1})

Figure 2. Same as Figure 1 but for the $v_{ej} = -453$ km s^{-1} ($z_{abs} = 2.649510$) absorption system in the spectrum of Q1009+2956.
(A color version of this figure is available in the online journal.)

and a weaker component is found at ~ 325 km s^{-1}. The central component shows an asymmetry, indicating the need for two Voigt components for an adequate fit. The feature at ~ 70 km s^{-1} in the Lyα panel cannot be Lyα belonging to this absorption system, since no counterpart is detected in the Lyβ panel. All three components of the N v profile show partial coverage, with coverage fractions between 0.33 and 0.43 (Table 2). The Lyβ component at 0 km s^{-1} is too strong relative to Lyα, indicating a blend that affects the Lyβ so that it can only be used as an upper limit. If saturated (and affected by partial coverage), Lyβ could have an equivalent width equal to that of Lyα, but it can never have a larger equivalent width. The O vi doublet lies in the Lyα forest, such that it is hard to evaluate whether it is detected for this system or not. If all of the detected absorption, either at 0 km s^{-1} or at 325 km s^{-1}, is due to O vi, the absorber would have a much larger coverage fraction than the N v, C iv, or Lyα absorbers at these same velocities. In our modeling, we will take the absorption lines coincident with O vi as an upper limit, but we note that the minima of the absorption at ~ 325 km s^{-1} in both members of the O vi doublet are at the same velocity as

those in the N v. Because of this, we will later consider whether viable single phase models can also explain this possible O vi absorption.

Transitions appearing in Figures 1–3, but not described above, provide limits for model constraints, either because they are not detected or because they are thought to be affected by blends.

3. PHOTOIONIZATION MODELING

Our calculations were performed with version 07.02.01 of Cloudy, last described by Ferland (1998). Our modeling assumes a series of plane-parallel slabs of gas (clouds) exposed to the ionizing continuum from the central engine. The gas within each absorbing cloud is assumed to have a uniform density, metallicity, and abundance pattern. In most cases, we assume a solar abundance pattern (Holweger 2001), so that for *every* element i, $A_i/A_{i,\odot} = Z/Z_\odot$ where $A_i = n_i/n_H$. When an adequate fit cannot be achieved using the solar abundance pattern, we consider deviations. The intensity of the ionizing
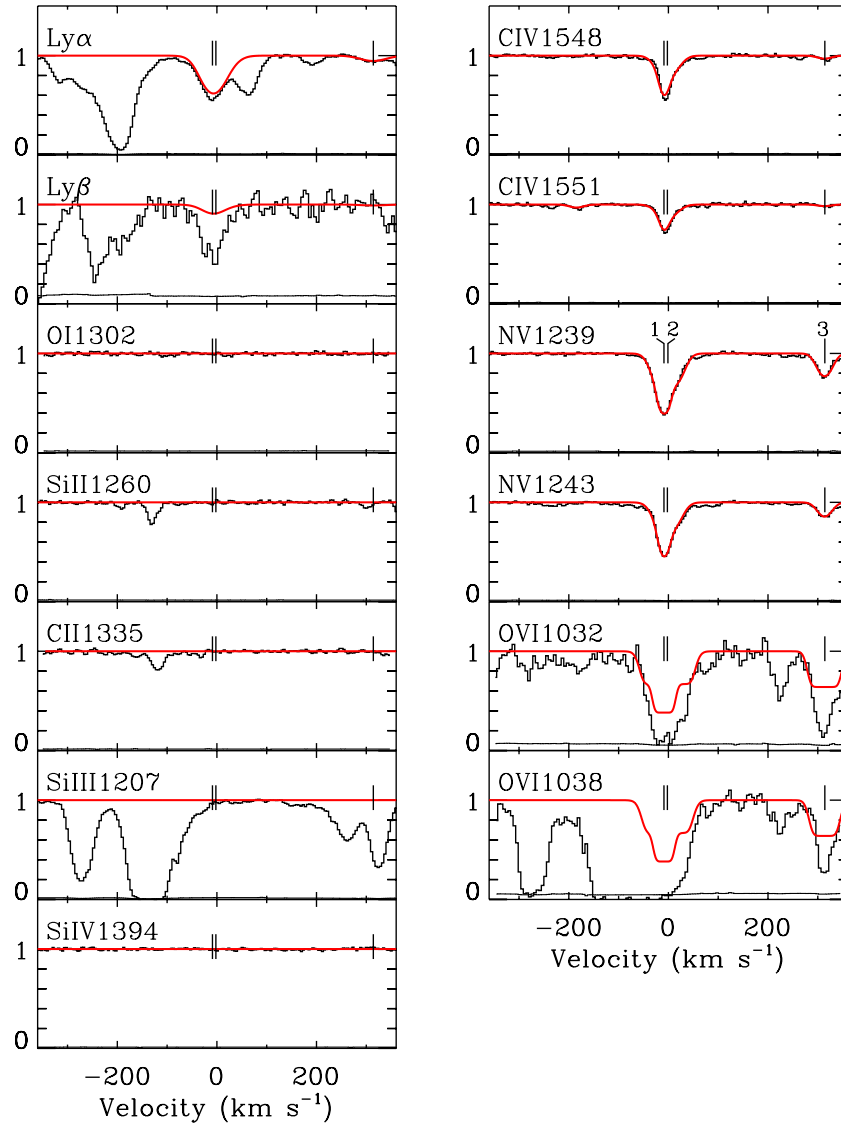
Figure 3. Same as Figure 1 but for the $v_{ej} = 764$ km s^{-1} ($z_{abs} = 2.7125$) absorption system in the spectrum of HS1700+6416.
(A color version of this figure is available in the online journal.)

continuum is parameterized by the ionization parameter,

$$U = \frac{n_\gamma}{n_H} = \frac{1}{4\pi r^2 c n_H} \int_{\epsilon_1}^{\epsilon_2} \frac{L_\epsilon}{\epsilon} d\epsilon, \qquad (1)$$

where r is the distance of the illuminated face of the cloud from the continuum source, ϵ_1 is the lowest energy required to photoionize the gas, i.e., $\epsilon_1 = 1$ Ry, and ϵ_2 is the high energy cutoff of the SED. In our model, we take $\epsilon_2 = 7.354 \times 10^6$ Ry. Each of our models is specified by U and n_H, which (given the quasar luminosity and spectral shape) corresponds to a given r. We also assume that all the ions within a cloud have the same coverage fraction, and that the gas cloud is in a state of thermal equilibrium, so it is parameterized by a single electron temperature, T_e. The assumption of the same coverage fraction for different lines is likely to be valid for those from ions with similar ionization states, particularly C IV and N V which are the most important constraints for out models. Lyα absorption may also arise from additional regions, but in any case will provide a lower limit on metallicity. In our favored models, the clouds are optically thin to the incident continuum so that the incident

SED does not change after the ionizing photons pass through an absorbing cloud.

We have measured the Doppler b parameters, column densities, and coverage fractions of the N V doublets, as we describe below, and optimized on these values (i.e., we required that Cloudy models produce them). We choose N V as the transition on which we optimize because it is located in a relatively "clean" spectral region where there are few blends. This allows us to determine its column density, Doppler parameter, and coverage fraction via Voigt profile fitting. The code AUTOVP (Dave et al. 1997) is used to derive an initial solution, and then MINFIT (Churchill 1997) is used to determine the minimum number of components that produce an adequate fit. The goal of the modeling exercise is to reproduce the observed absorption profiles for all other ions by adjusting three physical parameters: metallicity, $Z/Z_\odot$, ionization parameter, U, and hydrogen number density, n_H.

3.1. Voigt Profile Fitting of the N V Doublets

The approach of the MINFIT code is to first "overfit" the system using many Voigt components and then to reject
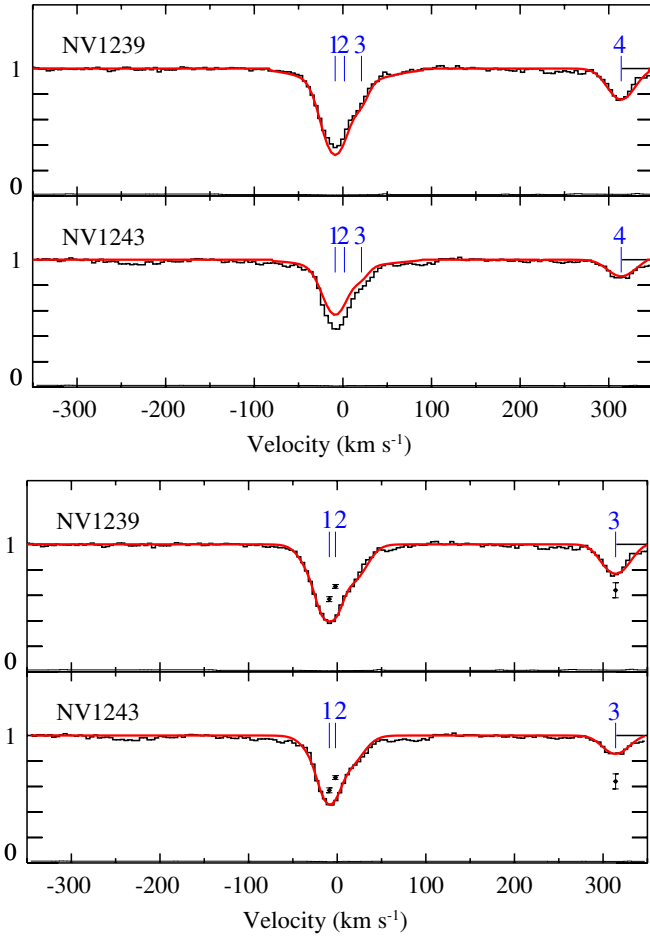
Figure 4. Voigt profile fits to the N v λλ1239, 1242 doublet in the $v_{ej} = 764$ km s^{-1} ($z_{abs} = 2.7125$) system in the spectrum of HS1700+6416. The velocity zero point is defined as in Figure 1. The fitting process minimizes the number of kinematic components needed for an adequate representation of the profile. Vertical ticks mark the component centers. In the upper pair of panels, the coverage factors of all components are fixed to be unity; in the lower pair of panels, the coverage factors of all components are treated as free parameters. Black dots with error bars represent the value of $(1 - C_f)$ for each component. Clearly, $C_f = 1$ does not provide an adequate fit, so that partial coverage is required.

(A color version of this figure is available in the online journal.)

components that do not improve the fits at a confidence level above 95%. This fitting technique has been used extensively in studies of intervening Mg II systems (e.g., Ding et al. 2003, 2005; Lynch et al. 2006). Table 2 lists the resulting fitting parameters. It is essential to include the coverage fractions as free parameters in the fitting process for these systems since $C_f = 1$ does not provide acceptable fits to these doublets within the observed uncertainties (Figure 4; Misawa et al. 2007).

3.2. Specification of the Ionizing Continuum

Although multi-band photometry and/or spectra of these three quasars are not available over the entire spectral range, some observational data are available to place constraints on the input SED. We consider three possible quasar SEDs.

1. A typical quasar SED from Elvis et al. (1994). This is a mean SED determined from 29 moderately luminous quasars.
2. A broken power-law SED from Mathews & Ferland (1987). This is a mean continuum determined by combining direct

Table 3
Spectral Indices of Different SED Models Compared to Observed Values

SED[a]	α_o	α_x	α_{ox}
Observed, HS1700+6416	−0.47	−1.00	−1.87
Elvis (1994)	−0.91	−0.93	−1.37
Mathews & Ferland (1987)	−0.50	−0.70	−1.41
Small BB I	−1.24	−0.99	−1.40
Small BB II	−1.27	−0.99	−1.60
Small BB III	−1.27	−0.99	−1.90
Medium BB I	−0.54	−1.00	−1.40
Medium BB II	−0.56	−1.00	−1.60
Medium BB III	−0.56	−1.00	−1.90
Big BB I	−0.49	−1.82	−1.40
Big BB II	−0.50	−2.30	−1.60
Big BB III	−0.51	−3.06	−1.90

Note. [a] The Roman numerals I, II, and III represent different values of α_{ox}.

observations, without distinguishing between radio-quiet and radio-loud quasars.

3. A multi-component continuum with either a small, a medium, or a big blue bump (BB; see the Cloudy document, *Hazy*, Ferland 2006, Section 6.2, for details), parameterized by $kT_{BB} = 10$ eV, 100 eV, and 300 eV, respectively (Casebeer et al. 2006). By adjusting the parameters of this prescription, we produce three different strengths of the BB, which we list in Table 3 ("small," "medium," and "big"). For each BB strength, we examine three different values of α_{ox} (denoted as I, II, and III in Table 3), which gives us nine different SED shapes for this model.

We utilize three parameters to constrain the SED: α_o, α_x, and α_{ox}, which are the UV/optical spectral slope, X-ray band spectral slope, and optical–X-ray spectral slope, respectively (assuming that $f_\nu \propto \nu^{+\alpha}$). The last is defined as $\alpha_{ox} = 0.3838 \log\left[\ell_\nu(2\,\text{keV})/\ell_\nu(2500\,\text{Å})\right]$, where $\ell_\nu(2\,\text{keV})$ and $\ell_\nu(2500\,\text{Å})$ are the monochromatic luminosities at 2 keV and at 2500 Å (Tananbaum et al. 1979).

The low-resolution ($R \sim 2000$) UV/optical spectrum of HS1700+6416 is available from the Data Release 5 (DR5) quasar catalog (Schneider et al. 2007) of the Sloan Digital Sky Survey (SDSS; York et al. 2000). We fitted the underlying continuum using a power law, with a small Balmer bump and the iron emission forest superimposed (D. E. Vanden Berk et al. 2010, in preparation), and obtained $\alpha_o = -0.47$ (see Table 3). This object was also observed by *Chandra* and *XMM-Newton*. The X-ray spectrum was adequately fit with a power-law index ~ -1 ($\alpha_x = -1.2 \pm 0.2$ for the *Chandra* spectrum and $\alpha_x = -1.1 \pm 0.2$ for the *XMM-Newton* spectrum; Misawa et al. 2008). Thus, we adopted $\alpha_x = -1$.

To find α_{ox}, we used the empirical correlation between it and the 2500 Å quasar luminosity (Vignali 2003; Strateva et al. 2005; Steffen et al. 2006). We adopt the α_{ox}–$\ell_\nu(2500\,\text{Å})$ relation by Steffen et al. (2006):

$$\alpha_{ox} = (-0.137 \pm 0.008) \log \ell_\nu(2500\,\text{Å}) + (2.638 \pm 0.240).$$

The 2500 Å luminosity is calculated as $\ell_\nu(2500\,\text{Å}) = 4\pi d_L^2 f_\nu(2500\,\text{Å})$, in which d_L is the luminosity distance and $f_\nu(2500\,\text{Å})$ is the rest-frame flux, derived from an extrapolation of the flux density at 4400 Å (Misawa et al. 2007) assuming $f_\nu \propto \nu^{-0.44}$ (Vanden Berk et al. 2001). Thus, for HS1700+6416 we find $\alpha_{ox} = -1.87$
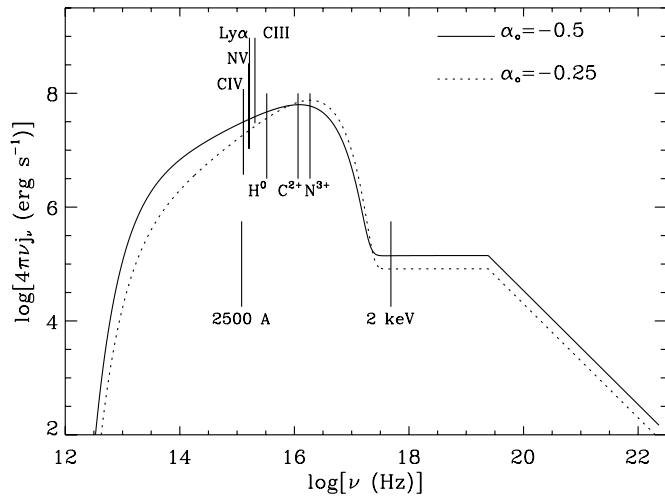
Figure 5. Shapes of two SEDs we used as input to our photoionization models. The solid line shows the SED used for HS1700+6416 while the dotted line shows the SED used for the other two quasars. These SEDs are normalized to an ionization parameter $\log U = 0.1$ for a hydrogen density of $\log (n_H/cm^{-3}) = 8$. Thus, they have the same photon luminosity between 1 and 7.354×10^6 Ry. Also labeled are positions of important transitions—Lyα, N v $\lambda\lambda 1239$, 1242 and C iv $\lambda\lambda 1548$, 1550. We also mark the photon frequencies needed to ionize N^{+3} to N^{+4}, C^{+2} to C^{+3}, and H^0 to H^+. We also mark the frequencies corresponding to 2500 Å and 2 keV since flux densities at these two frequencies are used to define α_{ox}.

The three spectral indices for HS1700+6416, from spectroscopic observations, are compared to those for possible quasar SEDs (Table 3). We find that the medium BB III SED best matches the observational constraints thus, we use this SED as the input ionizing flux for HS1700+6416. This SED is plotted as a solid line in Figure 5.

We measured α_o of the other two quasars from the low-resolution spectra of Q1009+2956 (Burles & Tytler 1998) and HE0130−4021 (Osmer et al. 1994), respectively. These UV/optical power-law indices are determined by connecting two empirical "line-free" regions redward of the Lyα emission line and are ~ -0.25 for both quasars. The 2500 Å luminosities for these two quasars are determined in the same manner as for HS1700+6416 and their α_{ox} values are both ~ -1.8. There have not been any X-ray spectral observations of Q1009+2956 or HE0130−4021 so, we assume they have the same α_x as HS1700+6416. Generally, the photoionization cross section decreases rapidly with photon energy so the ionization state is not sensitive to the X-ray spectral slope. We then also use the medium BB III multi-component SED for both of these quasars, but we adjust the optical slope to -0.25 to match the observations. This SED is shown as a dotted line in Figure 5.

We have integrated the above SEDs to compute the bolometric luminosities and ionizing ($E > 1$ Ry) photon rates for the three quasars (L_{bol} and Q, respectively). We first normalized them to match the 4400 Å luminosity density of each quasar (using the flux density and luminosity distance from Table 1). The resulting values are listed in Table 1; they will be useful for our estimates of the properties of the absorbing gas in Section 6.2.

3.3. Comparison of Cloudy Model Results to the Data and the Role of the Coverage Fraction

Cloudy calculates the electron temperature based upon thermal and ionization balance. Using this temperature, we calculate the microturbulence velocity for N v based on its observed total Doppler b parameter assuming that both of them follow

Gaussian distribution. We then calculate the b parameters for all other elements by combining this turbulent b with the thermal b, calculated from the atomic weight and the electron temperature. Using these b parameters and the column densities of each ion, output by Cloudy, we synthesize noiseless model spectra, convolving with a Gaussian function which represents the instrumental profile. We compare the theoretical profiles with the observed ones using a χ^2 test in combination with visual inspection. The wavelength range within which χ^2 is evaluated is carefully chosen because even a single pixel affected by a blend or an instrumental a artifact can dominate the χ^2 values.

We apply a grid method in $(Z/Z_\odot)$–U–n_H space to search for acceptable solutions by comparing model profiles to the observed absorption lines. In order to better visualize the models and compare them to the observed spectra, we take constant-n_H slices and examine combinations of $(Z/Z_\odot)$ and U in this two-dimensional parameter space. The ranges of $(Z/Z_\odot)$, U, and n_H we explore vary depending on the specific system, but typically they span $1 \lesssim \log(Z/Z_\odot) \lesssim 3$,[5] $-1.5 \lesssim \log U \lesssim 1.5$, and $2 \lesssim \log(n_H/cm^{-3}) \lesssim 14$. The initial increments are $\Delta \log(Z/Z_\odot) = 0.1$, $\Delta \log U = 0.1$, and $\Delta \log(n_H/cm^{-3}) = 2$. Finer grids are applied only if necessary. We assume that different kinematic (Voigt) components represent different parcels of gas, which we model separately. However, if kinematic components are blended together, we start by assuming that they are all described by the same model parameters. We refer to such models as the "initial" or "preliminary" models. After finding the best preliminary solution, we vary $(Z/Z_\odot)$ and U for each kinematic component within 0.2 dex of their preliminary values to seek better solutions with smaller χ^2 values.

In the process of producing synthetic line profiles for comparison to the observed spectra, we make use of the coverage fraction inferred from the relative strengths of the lines in the N v doublet (see Table 2). Since C_f represents the fraction of photons from the background source that pass through the absorber, we effectively dilute all the absorption lines of a given system by a factor equal to C_f. We have to assume that the same value of C_f applies to all transitions for lack of additional information. This need not be the case in general, however; Misawa et al. (2007) do find cases where different resonance doublets in the same system yield different values of C_f, for example. In one of our three quasars, HS1700+6416, we do have separate measurements of C_f for the N v and C iv doublets but they agree with each other within uncertainties. We return to the issue of the covering factor in Section 5 where we discuss the possibility of the absorbers covering different fractions of the continuum and broad emission line sources.

4. PHOTOIONIZATION MODEL RESULTS

4.1. HE0130−4021

This absorption complex can be described by nine kinematic components (Figure 1 and Table 2). These components are blended so we model them by first assuming that they are described by the same model parameters. Si iv $\lambda 1394$ is not detected, which yields a lower limit on $\log U$. Although O vi $\lambda\lambda 1032$, 1038 and C iii $\lambda 977$ do not provide strong constraints, we require that they are not overproduced by our models. The Lyα line provides a strong constraint for this system. Because the

---

[5] In our initial simulations, we tried to reproduce the absorption line strengths with $\log(Z/Z_\odot) \lesssim 1$. However, we found that acceptable models require relatively high metallicities, which led us to adopt this range of values in our grid search.
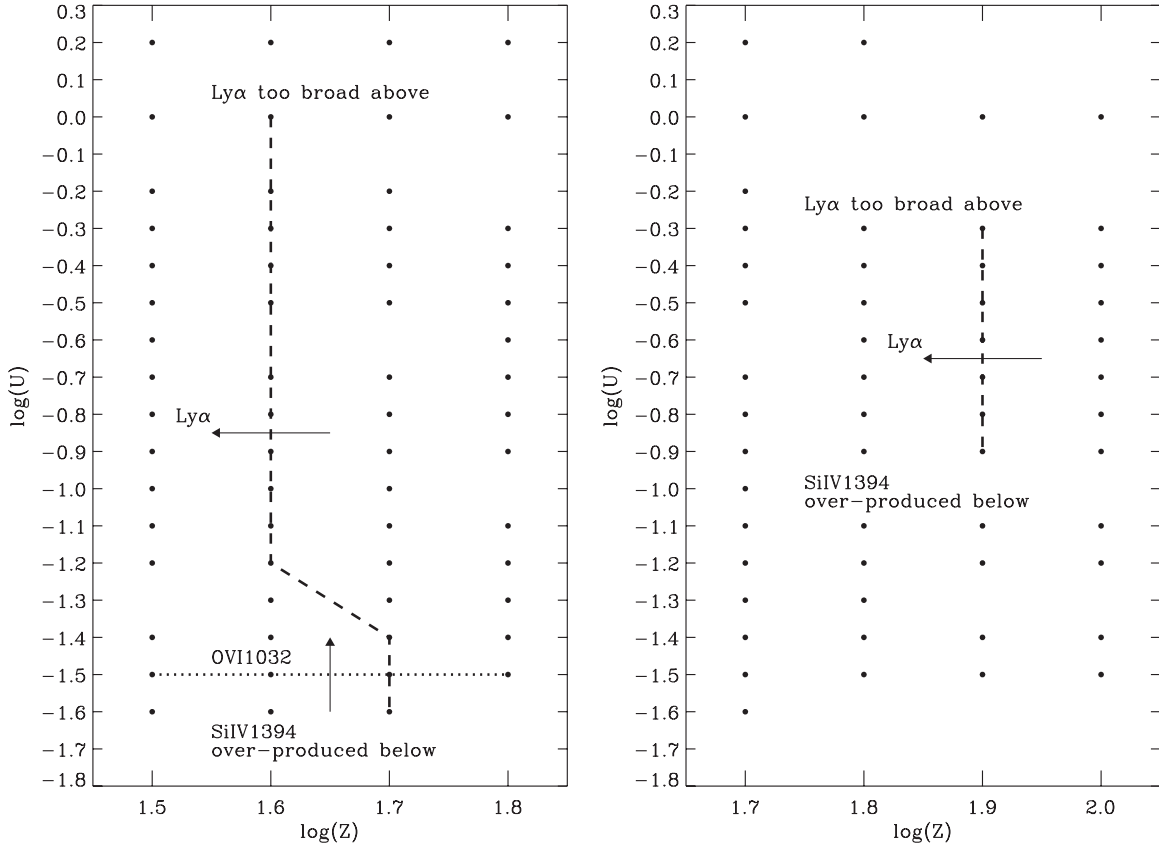
Figure 6. $\log(Z/Z_\odot)$–$\log U$ parameter slice at $\log n_H = 8$, showing the tracks of acceptable preliminary models for the absorption system in the spectrum of HE0130−4021. The left panel shows the tracks for the blue group (kinematic components 1−4, and 9). The right panel shows the tracks for the red group (kinematic components 5−8). Black dots are the cases we covered in our modeling. The dashed line represents the best-fit track for Lyα while the dotted line represents the best-fit track for O VI. Arrows indicate the directions in which a specific theoretical absorption profile becomes stronger, so on the "tail" side, the absorption line is underproduced while on the "head" side, it is overproduced.

saturated absorption troughs around 50 km s^{-1} and 100 km s^{-1} are not seen in Lyβ, they cannot be due to Lyman absorption from this system. These two absorption features actually divide the whole Lyα absorption system into a red part (positive velocity) and a blue part (negative velocity), which we can model separately. The blue part comprises components 1–4 and 9 while the red part consists of components 5–8. Although this system comprises many kinematics components, we can still obtain robust results for the coverage fraction of each component. This is because we fit the blue and red member doublets simultaneously so that only features appearing in both doublets contribute to the determination of C_f. The resulting relative uncertainties (listed in Table 2) are typically of order 20%, which includes errors in profile fitting as well as errors in continuum fitting.

We start by seeking models that can reproduce the observed Lyα absorption complex. For either the red or the blue part of the profile, we can find a series of solutions for $\log(Z/Z_\odot)$ and $\log U$ on a constant-n_H slice. Figure 6 illustrates the methodology we apply to all systems: it shows the acceptable models for Lyα for $\log(n_H/\text{cm}^{-3}) = 8$ and a range of $\log(Z/Z_\odot)$ and $\log U$. The highest and lowest possible values of $\log(Z/Z_\odot)$ and $\log U$ for different values of $\log(n_H/\text{cm}^{-3})$ are tabulated in Table 4. The blue and red parts of the profile yield different sets of acceptable model parameters. Figure 6 presents constraints on models based on the observed O VI λ1032 and Si IV λ1394 lines. The effect of changing $\log U$ and $\log(Z/Z_\odot)$ on the model profiles of Si IV λ1394 and Lyα is illustrated in Figures 7(a) and

(b). The O VI λ1032 profile is very insensitive to metallicity as well as to $\log U$ when $\log U \gtrsim -1.5$. Below this value, the O VI λ1032 absorption decreases gradually. Because the O VI doublet is in the Lyα forest, we use it as an upper limit on the O VI absorption that a model should produce. However, at $\log U \sim -1.5$, the red parts of O VI 1032,1038 can be adequately fit. Therefore, the intersection between the acceptable models for the red part of Lyα and the acceptable models for OVI 1032 happens at $\log U \sim -1.5$ and $\log(Z/Z_\odot) \sim 1.7$. This model also fits the observed C III λ977 absorption and it does not overproduce Si IV λ1394. For the blue part of the system, within the range of models that are consistent with the Lyα and SiIV 1394, the O VI λ1032 is never overproduced. Since the O VI is taken as an upper limit, these models are all considered acceptable, as listed in Table 4.

The synthesized line profiles are consistent with the data for values of $\log(n_H/\text{cm}^{-3})$ between 2 and 14. The ranges of $\log(Z/Z_\odot)$ and $\log U$ are slightly different for different $\log n_H$ values (Table 4). An example of an acceptable model is presented in Figure 1.

There are still discrepancies between the model and the observed spectrum of Lyα. Perhaps the Lyα line is blended with another transition because the corresponding absorption trough is not seen in Lyβ. The $v \sim 300$ km s^{-1} absorption trough in the Lyα window is also underproduced, which seems to suggest an additional weak component with a small Doppler parameter. Most of the absorption in O VI is underproduced by this model, with the exception of that at $v \sim 0$ km s^{-1}. The absorption at
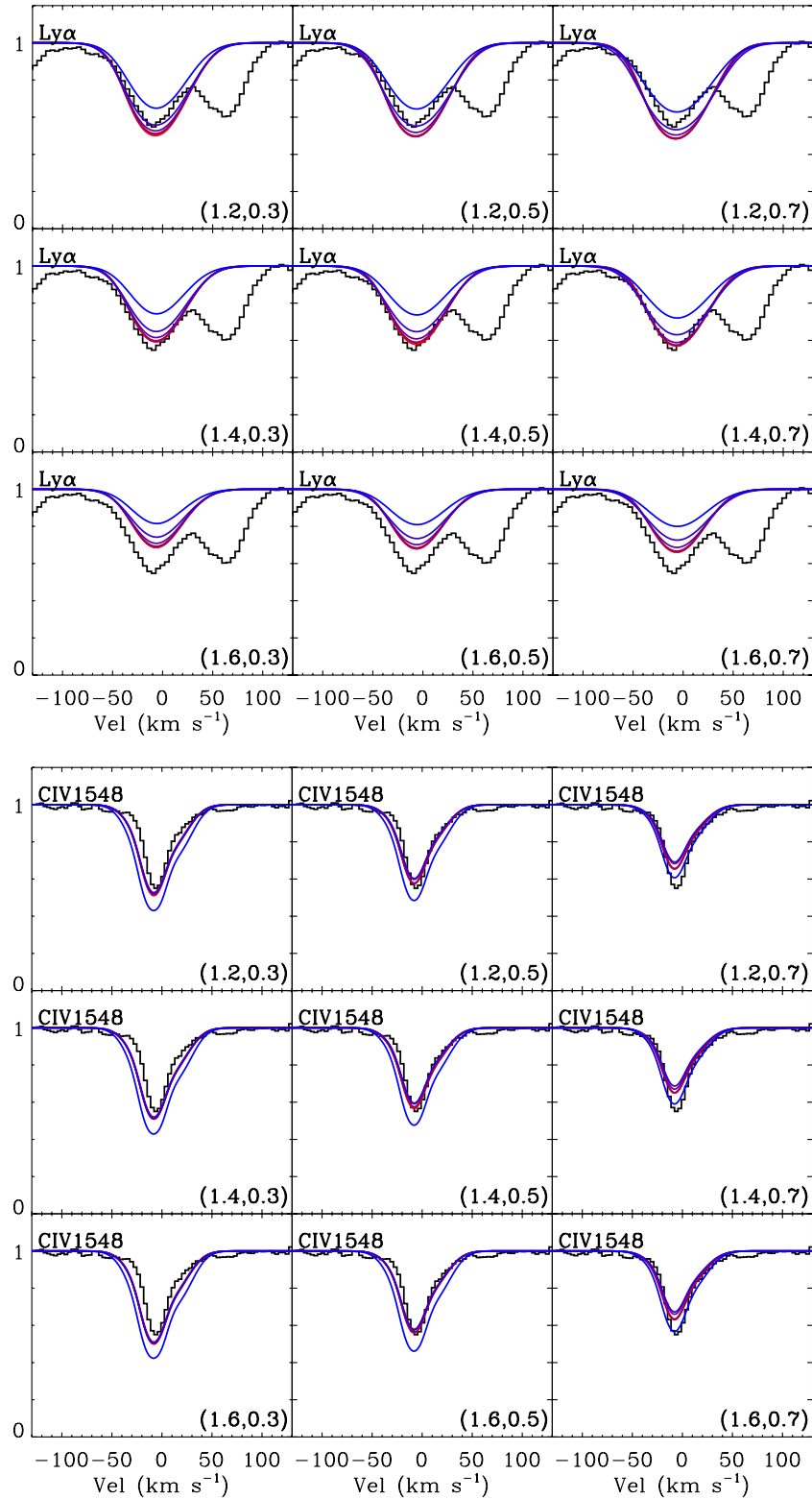
Figure 7. Plots of observed and synthesized profiles of the two central kinematic components of Lyα (e) and C IV λ1548 (f) for the absorption system in the spectrum of HS1700+6416. The different panels show how the models change as $(\log(Z/Z_\odot), \log U)$ vary about (1.4, 0.5). In each panel, the profiles are color-coded according to density in the same way as Figure 7(c). Figures 7(a)–(d), (g), and (h) are available in the online version of the journal.

(A color version and an extended version of this figure are available in the online journal.)

this velocity is mainly contributed by component 9, which is the only component with a coverage fraction of unity. We have assumed that the O VI absorption is only an upper limit, but if it is real, a separate phase would be required that has a larger coverage fraction. In the other two systems O VI is similarly underproduced; we discuss this further in Section 4.4.

We have attempted to optimize the model parameters for each kinematic component separately but we found that this

Table 4
Summary of Preliminary Fitting Results

Quasar	Kinematic Component	$\log(Z/Z_\odot)$	$\log U$	$\log(n_H/\mathrm{cm}^{-3})$	Abundance Pattern
HE0130−4021[b]	1–4,9	1.6	−0.6 to 0	2	Solar
		1.6–1.7	−1.4 to 0	8	Solar
		1.5–1.6	−1.4 to −0.3	10	Solar
		1.5	−1.3	12	Solar
		1.3	−1.0	14	Solar
	5–8	⩾1.7	⩾ − 0.6	2	Solar
		1.9	−0.9 to −0.2	8	Solar
		⩾1.8	−0.8 to 0.4	10	Solar
		1.6	−0.8	12	Solar
		1.8	−0.6	14	Solar
Q1009+2956	1–3	2.5	0.2	2–8	Solar, [S/H] ⩽ 1.5
		2.5	0.3	9	Solar, [S/H] ⩽ 1.5
		2.4	0.2	10	Solar, [S/H] ⩽ 1.4
		2.3	0.3	11–12	Solar, [S/H] ⩽ 1.5
		2.3	0.7	12	Solar, [C/H] ∼ 2.8
		2.5	0.4	13	Solar, [S/H] ⩽ 1.5
HS1700+6416[a]	1–2	1.4	0.5	2–8	Solar
		1.3	0.4	9	Solar
		1.3	0.5	10	Solar
	3	1.7	1.0	2–8	Solar

Notes. Here, we assume that blended kinematic components, as indicated in the second column of the table, are described by the same combination of model parameters.
[a] The results presented in this table are also a summary of the final results for this quasar. See the discussion in Section 4.1 of the text.

exercise did not yield useful results. We found a large number of "pockets" in parameter space, spanning a wide range of parameter values, where an acceptable fit can be achieved but there is no strong reason to prefer one particular "pocket" over the others. We attribute this outcome to the fact that the Lyman series lines that we use as constraints are blended with other lines and the profile of C III has a relatively low signal-to-noise ratio. Therefore, Table 4 provides the final summary of acceptable model parameters.

4.2. Q1009+2956

The absorption-line profile of this system can be reproduced using three kinematic components (Figure 2 and Table 2), which are blended together. In addition to N v, there are three main constraints: Lyα, C III λ977, and S VI λ933. We initially assume that the three components have the same parameters. We find that using a solar abundance pattern, we can always find overlapping regions in parameter space between the best fits of Lyα and C III λ977 if $\log(n_H/\mathrm{cm}^{-3}) \lesssim 13$. These solutions are at $2.3 \lesssim \log(Z/Z_\odot) \lesssim 2.5$ and $0.2 \lesssim \log U \lesssim 0.4$, (Figures 7(c) and (d)). However, we cannot find any overlapping parameter combinations between suitable fits for S VI λ933 and C III λ977. The S VI λ933 solutions also do not intersect with acceptable Lyα solutions, except when $\log(n_H/\mathrm{cm}^{-3}) \approx 12$. For most densities, only if we lower the sulfur abundance by about 1 dex (relative to the solar abundance pattern) can we obtain acceptable model profiles for all three of the constraints (Table 4). In the case that the absorption at the position of S VI λ933 is contaminated by blends with unrelated lines, an even larger sulfur abundance reduction would be required. In principle, it is possible to produce less S VI λ933 by increasing the nitrogen abundance, since N v is the optimized transition, however we find that such an adjustment is not sufficient to fully resolve the discrepancy. For the special case of $\log(n_H/\mathrm{cm}^{-3}) \approx$

12, the S VI λ933 and Lyα profiles can both be reproduced for $\log(Z/Z_\odot) \sim 2.3$ and $\log U \sim 0.7$. For that case, with a higher ionization parameter, an alternative acceptable model is found if we raise the carbon abundance by 0.5 dex, leaving the sulfur abundance unchanged from the solar pattern. These results are summarized in Table 4.

We next tune separately the metallicity and ionization parameter of each component, assuming that all three components have the same volume density, but allowing this common value of the density to vary. We select the best model parameters at each volume density value using χ^2 technique and visual inspection (Table 5). An example of acceptable models is presented in Figure 2. To obtain this improved fit, we vary the metallicities and ionization parameters of different components over a range about 0.2 dex. Through this exercise, we require that S VI λ933 is not overproduced. The left wing of Lyα cannot be well modeled and probably requires another component which may not be detected in metal-line absorption or may be related to a region to the blue of the N v λ1239 profile. We had neglected that in our fit, since we could not consider whether it was consistent with N v λ1243. Nevertheless, the modeling results for this system indicate metallicities considerably higher than the solar values.

4.3. HS1700+6416

This absorption system can be described by three kinematic components (Figure 3 and Table 2). Because the third component, at $v \sim 315$ km s^{-1}, is well separated from the central two components, we determine its parameters independently. Assuming the central two clouds to have the same parameters, the preliminary best fits, consistent with both Lyα and C IV λ1548 as well as with undetected transitions, are tabulated in Table 4. In Figures 7(e) and (f), we plot the profiles of the two central components of Lyα and C IV in the $\log(Z/Z_\odot)$–$\log U$ parameter

Table 5
Best Model Parameters for the Q1009+2956 Absorption Systems

Kinematic Component	$\log(Z/Z_\odot)$	$\log U$	$\log(n_H/\text{cm}^{-3})$	Abundance Pattern	r^a (pc)
1	2.4	0.0		Solar, [S/H] = 1.3	
2	2.6	0.3	2–8	Solar, [S/H] = 1.5	10–10000
3	2.3	0.0		Solar, [S/H] = 1.4	
1	2.3	0.1		Solar, [S/H] = 1.3	
2	2.5	0.3	9	Solar, [S/H] = 1.5	∼0.2
3	2.7	0.1		Solar, [S/H] = 1.7	
1	2.4	0.0		Solar, [S/H] = 1.4	
2	2.5	0.3	10	Solar, [S/H] = 1.5	∼0.8
3	2.3	0.0		Solar, [S/H] = 1.3	
1	2.2	0.2		Solar, [S/H] = 1.2	
2	2.4	0.3	11–12	Solar, [S/H] = 1.4	0.04–0.2
3	2.4	0.5		Solar, [S/H] = 1.4	
1	2.2	0.5		Solar, [C/H] = 2.7	
2	2.4	0.8	12	Solar, [C/H] = 2.9	∼0.04
3	2.5	0.5		Solar, [C/H] = 3.0	
1	2.7	0.3		Solar, [S/H] = 1.7	
2	2.6	0.5	13	Solar, [S/H] = 1.6	∼0.004
3	2.6	0.4		Solar, [S/H] = 1.6	

Note. [a] The distance of the absorbing gas from the ionizing source for this combination of U and n_H.

slice around this preliminary best fit for $\log(n_H/\text{cm}^{-3}) = 2, 4, 6, 8, 10,$ and 12. For $2 \lesssim \log(n_H/\text{cm}^{-3}) \lesssim 8$, the line strengths are almost independent of density, but for higher densities we see weaker Lyα and slightly stronger C IV absorption. When $\log(n_H/\text{cm}^{-3}) \gtrsim 11$, the acceptable fits to C IV $\lambda1548$ occur at $\log U \sim 0.6$, but Lyα is underproduced by the models so that it is impossible to obtain an acceptable fit at these very high densities. Observationally, variability on a timescale of 6.5 months in the quasar's rest frame implies $\log(n_H/\text{cm}^{-3}) > 3$ (based on considerations of the recombination time; see Section 2).

To refine our preliminary models, we next allow the central two components to have different parameters. Thus, we adjust $\log(Z/Z_\odot)$ and $\log U$ of each cloud separately, within ±0.2 dex of the preliminary best fit. A complete tabulation of the best model parameters at each value of the volume density can be found in Table 6. Take $\log(n_H/\text{cm}^{-3}) = 8$ for example, a better fit is found at $\log(Z/Z_\odot) = 1.3$, $\log U = 0.5$ for the first component and $\log(Z/Z_\odot) = 1.6$, $\log U = 0.6$ for the second component. Even for this example, shown in Figure 3, the Lyα components at $v \sim 0$ km s^{-1} are slightly underproduced. This may imply that an additional component would be needed, or that the Lyα is blended with a line from a system at another redshift. The latter is not unlikely given the unidentified component present at $v \sim 70$ km s^{-1}.

The best fit for the third kinematic component at $v \sim 315$ km s^{-1} is achieved at $\log(Z/Z_\odot) = 1.7$, $\log U = 1$ at $\log(n_H/\text{cm}^{-3}) = 2$–8. We cannot obtain any acceptable fits for $\log(n_H/\text{cm}^{-3}) > 8$ because model Lyα profiles become broader than the observed profiles for cases that match the observed C IV (Figures 7(g) and (h)). Combining all three components, Figure 3 shows one of the acceptable fits we obtain for this system.

4.4. The O VI Doublet

The energy required to produce O VI is much higher (8.371 Ry) than C IV (3.520 Ry) and N V (5.694 Ry). Thus, the O VI doublet probes highly ionized gas and could, in fact,

Table 6
Best Model Parameters for the HS1700+6416 Absorption Systems

Kinematic Component	$\log(Z/Z_\odot)$	$\log U$	$\log(n_H/\text{cm}^{-3})$	Abundance Pattern	r^a (pc)
1	1.3	0.5		Solar	
2	1.6	0.6	2–8	Solar	9–9000
1	1.2	0.5		Solar	
2	1.5	0.6		Solar	∼1
3	1.7	1.0	2–8	Solar	5–5000

Note. [a] The distance of the absorbing gas from the ionizing source for this combination of U and n_H.

arise in a more tenuous gas that is not co-spatial with the gas responsible for the lower-ionization absorption lines and also has a different coverage fraction of the background source(s). With the above in mind, we note that in the case of HS1700+6416 (Figure 3), the best model cannot fully reproduce the O VI absorption in both the central and redward components. This could signal that the O VI absorber has a larger coverage fraction. Another possibility is that the O VI is contaminated by lines from the Lyman forest, which is supported by the large widths of the "black" troughs around the O VI $\lambda1038$ line of HS1700+6416 and Q1009+2956 (Figures 2 and 3). Almost all spectral regions around O VI for the three quasars have some indication of blending, which makes the comparison of the synthesized O VI doublet profile to the data ambiguous. Therefore, we can only use the observed O VI absorption troughs to set an upper limit on the absorption produced by our models.

5. PARTIAL COVERAGE OF CONTINUUM AND BROAD EMISSION LINE REGIONS

In principle, the intrinsic absorbers could cover different fractions of the continuum source and the BELR (e.g., Ganguly et al. 1999). Thus, an absorption line superposed on a broad

emission line represents the absorption of different fractions of emission-line and continuum photons. If this is true, the coverage fraction one obtains from fitting a doublet is an *effective* coverage fraction, which represents the fraction of the photons from all the background sources that pass through the absorber. Thus, for an absorption line that is superposed on a broad emission line and the continuum, a more general expression for the normalized residual flux at a certain velocity is given by Ganguly et al. (see 1999)

$$R(v) = 1 - \frac{[1 - e^{-\tau(v)}][C_c(v) + W(v)\,C_e(v)]}{1 + W(v)} \quad (2)$$

(see also the discussion and more general formalism in Gabel et al. 2005). In the above expression, C_c and C_e represent the coverage fractions of the continuum source and of the BELR and $W = f_e/f_c$ is the ratio of the flux contribution of the emission line (without continuum) and the continuum only at the position of the absorption line. In principle, C and W are functions of velocity across the absorption-line profile. However, since the absorption lines of interest here are fairly narrow, W does not change appreciably over the profile of the absorption line and we can regard it as independent of velocity. By rearranging Equation (2), one can show that the effective coverage fraction, C_f, can be expressed as the weighted average of C_e and C_c as

$$C_f = \frac{C_c + W C_e}{1 + W}. \quad (3)$$

In practice, we can determine C_f by fitting the profiles of the UV resonance doublets and W by measuring the strength of the broad emission line relative to the continuum at the location of the absorption doublet. This leads to a relation between C_e and C_c but it does not allow us to determine C_e and C_c separately. An example of a graphical depiction of this relation can be found in Figure 10 of Ganguly et al. (1999).

The N v absorption doublet presents a further complication because it is likely to be superposed on the *blend* of the Lyα and N v emission lines. The regions emitting Lyα and N v are likely to have a different spatial extent and their coverage fractions should also be different. This is suggested by the results of reverberation mapping studies (see, for example, Peterson & Wandel 2000; Onken & Peterson 2002; Kollatschny 2003), which indicate an ionization stratification in the BELR. Under these circumstances, in the numerator of Equations (2) and (3), we must replace $W C_e$ by $W_{\mathrm{Ly\alpha}} C_{\mathrm{Ly\alpha}} + W_{\mathrm{N\,v}} C_{\mathrm{N\,v}}$ and in the denominator, we must replace W by $W_{\mathrm{Ly\alpha}} + W_{\mathrm{N\,v}}$. In this new notation $C_{\mathrm{Ly\alpha}}$ and $C_{\mathrm{N\,v}}$ are the coverage fractions of the Lyα and N v emitting regions and $W_{\mathrm{Ly\alpha}}$ and $W_{\mathrm{N\,v}}$ are defined in a manner analogous to the definition of W.

Putting aside the above complication, we can invert Equation (3) to obtain an expression for C_c, in terms of C_f, W, and C_e. However, since C_e is unknown in practice, this relation can only lead to upper and lower bounds on C_c, corresponding to $C_e = 0$ and 1, respectively. Even if the absorption doublet is superposed on a blend of emission lines, the expression for C_f reduces to Equation (3) if the BELR is fully covered or not covered at all. Taking the error bars on the measured quantities into account, we obtain the following expressions for the limits on C_c:

$$C_c^{\max} = \min\{1,\ [1 + (W + \delta_W)](C_f + \delta_{C_f})\} \quad \text{and} \quad (4)$$

$$C_c^{\min} = \max\{0,\ [1 + (W - \delta_W)](C_f - \delta_{C_f}) - (W + \delta_W)\},$$

where δ_X denotes the error bar on X.

Table 7
Constraints on Continuum and BELR Coverage Fractions

Quasar	Ion	W^a	C_c	C_e
HE0130−4021	N v	1.1 ± 0.4	Unconstrained	...
			<0.5	...
			Unconstrained	...
			<0.4	...
			<0.3	...
			<0.4	...
			Unconstrained	...
			<0.6	...
			>0.3	...
	Lyα $(C_f = 0.3)^b$	0.5 ± 0.3	Unconstrained	Unconstrained
Q1009+2956	N v	0.66 ± 0.12	Unconstrained	...
			>0.2	...
			<0.5	...
	Lyα $(C_f = 0.5)^b$	1.2 ± 0.2	<0.6	Unconstrained
HS1700+6416	N v	0.96 ± 0.06	0.2–0.8	...
			<0.7	...
			<0.8	...
	Lyα $(C_f = 0.4)^b$	0.6 ± 0.2	<0.7	>0.2
	C iv	0.41 ± 0.02	0.2–0.8	>0.4

Notes.
[a] The values of W were obtained from the following spectra: for HE0130−4021 we used the spectrum published by Osmer & Smith (1976), for Q1009+2956 we used the spectrum published by Burles & Tytler (1998), and for HS1700+6416 we used the SDSS DR5 spectrum.
[b] In the case of Lyα we cannot determine C_f from the data, therefore we assign a value equal to the average of all the N v kinematic components.

In an analogous manner, we can use Equation (3) to derive limits on C_e, using the fact that C_c must lie between 0 and 1. The corresponding expressions, including uncertainties on the measured quantities, are

$$C_e^{\max} = \min\left\{1,\ \frac{[1 + (W + \delta_W)](C_f + \delta_{C_f})}{(W - \delta_W)}\right\} \quad \text{and} \quad (5)$$

$$C_e^{\min} = \max\left\{0,\ \frac{[1 + (W - \delta_W)](C_f - \delta_{C_f})}{(W + \delta_W) - 1}\right\}. \quad (6)$$

We have used flux-calibrated, low-resolution spectra of the three quasars to measure the values of W for the Lyα, and N v absorption lines (as well as C iv absorption line in the case of HS1700+6416). Using these values of W and the values of C_f from Table 2, we have estimated the limits on the coverage fractions of the continuum source and the BELR, C_c and C_e, which we list in Table 7. Limits derived from the Lyα absorption line involve the assumption that the effective coverage fraction of the Lyα absorber is the average of the values measured for the N v absorber, which need not be correct. Nevertheless, these limits appear to be consistent with those derived from the N v and C iv doublets. The limits on the continuum coverage fraction derived from different N v kinematic components in the same quasar appear to be consistent with each other with one exception: component 9 of HE0130−4021, for which the effective coverage fraction is measured to be $C_f = 1$. The only reliable limit on the BELR coverage fraction comes from the C iv doublet of HS1700+6416.

A closely related issue is whether the superposition of absorption lines on strong emission lines dilutes their strengths

by different amounts and leads to large errors in our estimated abundances. The relative strengths of the Lyα and N v absorption lines are particularly sensitive to this effect, especially when the blueshift of the absorption lines is small. In a specific scenario where the absorber covers only the continuum source, the Lyα absorption line is superposed on the peak of the Lyα emission line and can be diluted much more than the N v line which is superposed on the red wing of the Lyα emission line (the velocity difference between the Lyα and N v absorption lines is approximately 5925 km s^{-1}). In such a case, the procedure we follow here to determine column densities, will lead us to underestimate the column density of Lyα relative to that of N v and our models would yield a nitrogen abundance that is higher than the true one.

Examining the values of W listed in Table 7, we see that if such a scenario is true, the N v absorption line is actually diluted more than the Lyα absorption line in HE0130−4021 and HS1700+6416. In other words, in these two quasars we would have underestimated the nitrogen abundance rather than overestimated it. To verify our expectation quantitatively, we explored a new set of models for HS1700+6416 in which we assumed that the absorber covers the continuum source but not the BELR. Thus, we started by adopting the C_f value of Cloud 2 because it is the dominant component and set $C_e = 0$ and $C_c = 0.64$ for all transitions. As a result, the *effective* coverage fraction for each transition depends on its W value, e.g., $C_f = 0.33$ for Nv, $C_f = 0.45$ for C IV, and $C_f = 0.34$ for Lyα. By setting $\log(n_H/cm^{-3}) = 8$, we find an acceptable fit at $(\log(Z/Z_\odot), \log U) = (1.6, 0.8)$. Compared to our best fit with $C_c = C_e$, this metallicity is 0.2 dex higher and the ionization parameter is 0.4 dex higher.

In Q1009+2956, we have the opposite situation, in which $W_{Ly\alpha}$ is larger than W_{NV}, i.e., Lyα is diluted more by emission line than N v, suggesting that metallicity may have been overestimated. To assess whether this is indeed the case, we explored a new set of models in which the C_e has the minimum value possible and C_c has the maximum value possible. According to Equations (4) and (6), these values are $C_c = 1$ and $C_e = 0.245$. Thus, the effective covering factors are $C_f = 0.593$ for Lyα, and $C_f = 0.895$ for C III. By setting $\log(n_H/cm^{-3}) = 8$, we find an acceptable model at $(\log(Z/Z_\odot), \log U) = (2.5, 0.4)$, very similar to our previous best-fitting model which had $C_c = C_e$.

In the calculation above, we assumed the same *average* value of W of two members of the N v doublets. However, the value of W could differ between the blue and red members of the N v doublet, which could affect not only the metallicity estimate but also values of the coverage fractions. In this particular case, however, the value of W is the same for the two members of the double, within uncertainties.

6. DISCUSSION

6.1. High Metallicities

One of the main results of this work is that the metallicities in intrinsic NAL systems are quite high, $\log(Z/Z_\odot) \gtrsim 1$. Several possible scenarios have been proposed to produce supersolar metallicities in the vicinity of the central massive black holes of quasars (Hamann & Ferland 1999). The most natural scenario involves normal galactic chemical evolution (see Hamann & Ferland 1992, 1993). By considering spectral synthesis and chemical enrichment models of the N v/C IV and

N v/He II emission line ratios, it was suggested that nitrogen is overabundant by factors of 2–9 in high-redshift ($z > 2$) quasars (Hamann & Ferland 1999). Highly evolved gas with $\log(Z/Z_\odot) > 0.5–1.1$ is needed to produce such a large overabundance of nitrogen. This evolutionary model requires a large number of high mass stars and implies a flat initial mass function (IMF) and rapid star formation. The power-law index of the IMF ($\Phi \propto M^\gamma$) can be in the range $\gamma = 0.9–1.4$ and star formation must occur in less than 0.5 Gyr for $z > 4$ objects (Hamann & Ferland 1992). This vigorous star formation is consistent with that found in the environment of active galactic nuclei (AGNs). The required timescales, metallicities, and IMFs are similar to those of elliptical galaxies and bulges of disk galaxies (Romano et al. 2002). Quasars with more massive host galaxies tend to be more metal rich, based on observations of massive ellipticals (Clemens et al. 2009; De Lucia et al. 2006). Therefore, the high abundances derived from our absorbing systems are not surprising, assuming this scenario. The quasars could undergo extensive chemical evolution before they are observable. Other possible processes within the accretion disk that can lead to supersolar metallicities include metal enrichment by star trapping (Artymowicz et al. 1992; Shields 1996), star formation (Collin & Zahn 1999; Goodman & Tan 2004), and non-stellar nucleosynthesis (Kundt 1996). However, it is unlikely that these mechanisms can produce metallicities as high as $\log(Z/Z_\odot) \sim 1$.

Early measurements of extremely high quasar metallicities based on BALs (Turnshek 1986) could have been overestimated because partial coverage of the background emission was not taken into account, leading to underestimation of column densities (Hamann & Ferland 1999). However, since our analysis of NALs takes partial coverage into account, our measurements do not suffer from this bias. Actually, supersolar metallicities have also been derived for associated absorption systems in low-redshift AGNs (Papovich et al. 2000; Fields et al. 2005; Gabel et al. 2006). However, those metallicities are not higher than $\log(Z/Z_\odot) \sim 1$, i.e., somewhat lower than our results for quasar intrinsic NAL systems. This difference could be due to the higher redshifts of our NAL systems and/or due to their presence in more luminous AGNs. Rapid and vigorous stellar evolution is likely to accompany quasar activity, as suggested by a correlation between the Eddington ratio and the BELR metal abundance spanning three orders of magnitude in both quantities (e.g., Shemmer et al. 2004). The resulting high-metallicity gas could then be diluted with a low-metallicity interstellar medium as it moves outward in the host galaxy. Eventually, it can escape the host-galaxy potential, enriching the interstellar and intergalactic medium.

It is also possible that we are looking only at the tip of the iceberg, i.e., at the most highly enriched gas. A diversity of absorber properties, including metallicity, has been reported by Petitjean et al. (1996). Not only can absorbers have different coverage fractions for the continuum and BELR but also different ions/species can have different coverage fractions due to the multi-phase structure of the gas. Different coverage fractions for different ions/species are also inferred from the general properties of the strong-C IV family of intrinsic NALs (Misawa et al. 2007), which usually have a saturated Lyα line, but no detected N v, implying a lower ionization state for the gas. In the strong-N v NAL systems studied in this paper, the O VI doublet may sometimes be underproduced by the models, which may be the result of a greater coverage fraction of the O VI absorber. Thus, the high metallicities that we derived for

the NAL gas in which N v is detected need not apply to all of the gas surrounding the central engine.

6.2. Properties of the Absorbing Gas

The ionization parameters that we obtained are similar to those for BALs. A typical value of a BAL ionization parameter is $\log U \sim 0$ (with a range of -1.0 to $+0.6$; e.g., Crenshaw et al. 2003; Wampler et al. 1995; Telfer et al. 1998). Both an intrinsic NAL and a BAL are observed in the spectrum of Q0059−2735 by Wampler et al. (1995), who show that both can be fitted with $\log U = -0.7$. Hamann (1998) finds that $\log U \gtrsim -0.6$ is required to model the BAL of PG 1254+047, while Telfer et al. (1998), using a two-slab geometry to model the BAL system of QSO SBS 1542 + 541, find $-1.1 < \log U < 0.6$ for the lower-ionization zone and $\log U \gtrsim 0.3$ for the higher-ionization zone.

If we assume that the outflow includes thin filaments (justified below) that are responsible for the UV absorption lines that we observe, we can estimate the outflow rate in these filaments as

$$\dot{M} = 4\pi r^2 \left(\frac{\delta r}{r}\right) \rho v \left(\frac{\delta \Omega}{4\pi}\right) , \qquad (7)$$

where ρ is the typical mass density of absorbing filaments, r is their typical distance from the center, δr is their typical thickness in the radial direction, and $\delta \Omega$ is the solid angle they subtend to the center of the flow. We can re-cast the above expression by using the definition of the ionization parameter, $U \equiv Q/4\pi r^2 n_H c$, to replace $4\pi r^2 \rho$ (Q is the rate of emission of ionizing photons at $E > 1$ Ry, and n_H is the hydrogen number density). We also note that the thickness of a filament is related to the hydrogen density, and radial column density, N_H, via $N_H = n \, \delta r$. Thus, we can write

$$\dot{M} = 5.2 \times 10^{-5} N_{18} \, v_2 \, f_{-1} \left(\frac{Q_{58}}{n_6 \, U}\right)^{1/2} M_\odot \, \text{yr}^{-1} , \qquad (8)$$

where $N_H = 10^{18} N_{18} \, \text{cm}^{-2}$, $v = 10^2 v_2 \, \text{km s}^{-1}$, $(\delta \Omega/4\pi) = 10^{-1} f_{-1}$, $Q = 10^{58} Q_{58} \, \text{s}^{-1}$, and $n_H = 10^6 n_6 \, \text{cm}^{-3}$. We also note that from the definition of the ionization parameter, we can obtain an estimate of the distance of the absorbing filament from the ionizing source.

To justify the assumption that the absorbers are thin, we note that using the definition of U and $N_H = n \, \delta r$, we obtain $\delta r/r = N_H^2 4\pi c U/n_H Q$. The values of N_H (neutral plus ionized) inferred from our photoionization models are in the following range: $\log(N_H/\text{cm}^{-2}) \sim 16$–19 for HE0130–4021, $\log(N_H/\text{cm}^{-2}) \sim 17$–18 for Q1009+2956, and $\log(N_H/\text{cm}^{-2}) \sim 19$ for HS1700+6416, the values of U are given in Tables 4–6 and the values of Q are given in Table 1. Thus, any combination of values of the above quantities yields $\delta r/r < 0.01$ which indicates that the absorbers are geometrically thin along the line of sight.

We can now use Equation (8) to obtain constraints on the mass outflow rate. The necessary values of N_H, v, U, and Q are given in Tables 4–6. We also use a value of $f_{-1} \sim 5$ based on the results of Misawa et al. (2007). Unfortunately, we have very poor constraints on the hydrogen volume density, which lead to a very wide range of values for the mass outflow rate, i.e., $\dot{M} \sim$ few $M_\odot \, \text{yr}^{-1}$ for the lowest densities and $\dot{M} < 10^{-4} \, M_\odot \, \text{yr}^{-1}$ for $n_H \geqslant 10^{10} \, \text{cm}^{-3}$. The kinetic power of these filaments is negligible compared to the electromagnetic luminosity ($\varepsilon_k \equiv \frac{1}{2}\dot{M} v^2/L_{\text{bol}} \lesssim 10^{-5}$), however they may be embedded in a hotter, more massive outflow or they may be

accompanied by a more massive outflow along a different line of sight.

Finally, we note that the poor constraints on the density also lead to poor constraints on the distance of the filament from the ionizing source, r. In Tables 5 and 6, we list the constraints on the radial distance of the filaments as a function of density for Q1009+2956 and HS1700+6416 (the results for HE0130–4021 are very similar). For $n_H \geqslant 10^9 \, \text{cm}^{-3}$, the absorbers turn out to be very close to the ionizing source, at distances comparable to the size of the BELR, while at the lowest densities, the filaments are located in the outskirts of the host galaxy.

7. SUMMARY AND CONCLUSIONS

In this paper, we modeled the intrinsic NAL systems in the spectra of the quasars HE0130−4021, Q1009 +2956, and HS1700+6416, We identify these systems as intrinsic because they exhibit partial coverage in the N v $\lambda\lambda$1239, 1242 doublet. Using the photoionization code Cloudy, we simulate and reconstruct each absorption feature observed in a system by adjusting the metallicity (relative to the Sun), $Z/Z_\odot$, ionization parameter, U and hydrogen volume density, n_H. Our main conclusions are as follows.

1. All three intrinsic systems have metallicities of $\log(Z/Z_\odot) \gtrsim$ 1–2, regardless of constraints on U or n_H. We find the high metallicities that we infer cannot alternatively be explained by different coverage fractions of the continuum source and BELR. The origin of these supersolar metallicities is unknown, but we speculate that they may result from intensive star formation before the quasar becomes observable. They could also be related to an inhomogeneous metallicity distribution in the vicinity of the quasar central engine.
2. All three intrinsic systems require high ionization parameters, $\log U \sim 0$, which are similar to those derived for BALs.
3. We can constrain the coverage fractions of the continuum source and the BELR separately, and find that the continuum source is not fully covered by the absorbers.
4. Although we cannot constrain the hydrogen volume density very well, we do find that the widths of the synthesized line profiles become larger than the observed ones at very high densities. This is a result of a sharp increase in temperature at high densities, produced by free–free absorption of infrared photons by free electrons. This leads us to conclude that the hydrogen volume density is in the range $2 \lesssim \log(n_H/\text{cm}^{-3}) \lesssim 9$.
5. As a result of the large range of possible densities, we cannot obtain robust estimates of the mass outflow rate in the filaments responsible for the N v absorption. We can conclude, nevertheless, that $\dot{M} \lesssim$ few $M_\odot \, \text{yr}^{-1}$, and the corresponding power is a negligible fraction of the electromagnetic luminosity.
6. The strength of the O vi $\lambda\lambda$1032, 1038 doublet is underproduced by the models that reproduce the other absorption lines. This suggests that the O vi lines are either contaminated by lines in the Lyman forest of that they arise in a separate gas phase with a larger coverage fraction.

The strong-N v absorbers studied in this paper make up one of two, apparently distinct, families of intrinsic absorber identified by (Misawa et al. 2007). Our next goal is to study the physical properties of the other family of absorbers, the strong-C iv family and probe the origin of the two families.

REFERENCES

Arav, N., Korista, K. T., Barlow, T. A., & Begelman, 1995, Nature, 376, 576

Arav, N., et al. 2007, ApJ, 658, 829

Artymowicz, P., Lin, D. N. C., & Wampler, E. J. 1992, ApJ, 409, 592

Barlow, T. A., Hamann, F., & Sargent, W. L. W. 1997, in ASP Conf. Ser. 128, Mass Ejection from Active Galactic Nuclei, ed. N. Aravm, I. Shlosman, & R. J. Weymann (San Francisco, CA: ASP), 13

Barlow, T. A., & Sargent, W. L. W. 1997, AJ, 113, 136

Brandt, W. N., Laor, A., & Wills, B. J. 2000, ApJ, 528, 637

Brotherton, M. S., De Breuck, C., & Schaefer, J. J. 2006, MNRAS, 372, L58

Burles, S., & Tytler, D. 1998, ApJ, 507, 732

Casebeer, D. A., Leighly, K. M., & Baron, E. 2006, ApJ, 637, 157

Chartas, G., et al. 2009, New Astron. Rev., 53, 128

Churchill, C. W. 1997, PhD thesis, Univ. California, Santa Cruz

Clemens, M. S., Bressan, A., Nikolic, B., & Rampazzo, R. 2009, MNRAS, 392, L35

Collin, S., & Zahn, J.-P. 1999, A&A, 344, 433

Crenshaw, D. M., Kraemer, S. B., & George, I. M. 2003, ARA&A, 41, 117

Dave, R., Hernquist, L., Weinberg, D. H., & Katz, N. 1997, ApJ, 477, 21

De Lucia, G., Springel, V., White, S. D. M., Croton, D., & Kauffmann, G. 2006, MNRAS, 366, 499

Ding, J., Charlton, J. C., Bond, N. A., Zonak, S. G., & Churchill, C. W. 2003, ApJ, 587, 551

Ding, J., Charlton, J. C., & Churchill, C. W. 2005, ApJ, 621, 615

D'Odorico, V., Cristiani, S., Romano, D., Granato, G. L., & Danese, L. 2004, MNRAS, 351, 976

Dunn, J. P., et al. 2010, ApJ, 709, 611

Elvis, M. 2000, ApJ, 545, 63

Elvis, M., et al. 1994, ApJS, 95, 1

Ferland, G. J. 2006, University of Kentucky Internal Report, 565

Ferland, G. J., Korista, K. T., Verner, D. A., Ferguson, J. W., Kingdon, J. B., & Verner, E. M. 1998, PASP, 110, 761

Fields, D. L., Mathur, S., Pogge, R. W., & Nicastro, F. 2005, ApJ, 634, 928

Gabel, J., Arav, N., & Kim, T. S. 2006, ApJ, 646, 742

Gabel, J., et al. 2005, ApJ, 623, 85

Ganguly, R., Bond, N. A., Charlton, J. C., Eracleous, M., Brandt, W. N., & Churchill, C. W. 2001, ApJ, 549, 133

Ganguly, R., & Brotherton, M. S. 2008, ApJ, 672, 102

Ganguly, R., Eracleous, M., Charlton, J. C., & Churchill, C. W. 1999, ApJ, 117, 2594

Ganguly, R., Masiero, J., Charlton, J. C., & Sembach, K. R. 2003, ApJ, 598, 922

Ghosh, K. K., & Punsly, B. 2007, ApJ, 661, L139

Giustini, M., Cappi, M., Chartas, G., Eracleous, M., Palumbo, G. G. C., & Vignali, C. 2010, in ASP Conf. Ser. 128, Mass Ejection from Active Galactic Nuclei, ed. N. Aravm, I. Shlosman, & R. J. Weymann (San Francisco, CA: ASP), 13

Goodman, J., & Tan, J. C. 2004, ApJ, 608, 108

Hamann, F. 1997, ApJ, 109, 279

Hamann, F. 1998, ApJ, 500, 798

Hamann, F. W., Barlow, T. A., Chaffee, F. C., Foltz, C. B., & Weymann, R. J. 2001, ApJ, 550, 142

Hamann, F., Dietrich, M., Sabra, B. M., & Warner, C. 2004, in Origin and Evolution of the Elements, Proc. Carnegie Obs. Centennial Symp., ed. A. McWilliam & M. Rauch (Camegie Obs. Astrophys. Series; Cambridge: Cambridge Univ. Press), 440

Hamann, F., & Ferland, G. 1992, ApJ, 391, 53

Hamann, F., & Ferland, G. 1993, ApJ, 418, 11

Hamann, F., & Ferland, G. 1999, ARA&A, 37, 487

Hamann, F., Korista, K. T., Ferland, G. J., Warner, C., & Baldwin, J. 2002, ApJ, 564, 592

Hamann, F., & Sabra, B. 2004, in ASP Conf. Ser. 311, AGN Physics With the Sloan Digital Sky Survey, ed. G. T. Richards & P. B. Hall (San Francisco: ASP), 203

Holweger, H. 2001, in AIP Conf. Proc. 598, Solar and Galactic Composition, ed. R. F. Wimmer-Schweingruber & P. Bochsler (Melville, NY: AIP), 23

Ivanchik, A. V., Petitjean, P., Balashev, S. A., Srianand, R., Varshalovich, D. A., Ledoux, C., & Noterdaeme, P. 2010, MNRAS, 404, 1583

Jones, T. M., Misawa, T., Charlton, J. C., Mshar, A. C., & Ferland, G. J. 2010, ApJ, 715, 1497

Kollatschny, W. 2003, A&A, 407, L61

Kundt, W. 1996, Ap&SS, 235, 319

Lynch, R. S., Charlton, J. C., & Kim, T.-S. 2006, ApJ, 640, 81

Mathews, W. G., & Ferland, G. J. 1987, ApJ, 323, 456

Mathur, S., Elvis, M., & Wilkes, B. 1995, ApJ, 452, 230

Misawa, T., Charlton, J. C., Eracleous, M., Ganguly, R., Tytler, D., Kirkman, D., Suzuki, N., & Lubin, D. 2007, ApJS, 171, 1

Misawa, T., Eracleous, M., Chartas, G., & Charlton, J. C. 2008, ApJ, 677, 863

Misawa, T., Eracleous, M., Charlton, J. C., & Tajitsu, A. 2005, ApJ, 629, 115

Murray, N., Chiang, J., Grossman, S. A., & Voit, G. M. 1995, ApJ, 451, 498

Narayanan, D., Hamann, F., Barlow, T., Burbidge, E. M., Cohen, R. D., Junkkaribeb, V., & Lyons, R. 2004, ApJ, 601, 715

Onken, C. A., & Peterson, B. M. 2002, ApJ, 572, 746

Osmer, P. S., Porter, A. C., & Green, R. F. 1994, ApJ, 436, 678

Osmer, P. S., & Smith, M. G. 1976, ApJ, 210, 267

Papovich, C., Norman, C. A., Bowen, D. V., Heckman, T., Savaglio, S., Koekemoer, A. M., & Blades, J. C. 2000, ApJ, 531, 654

Peterson, B. M., & Wandel, A. 2000, ApJ, 540, L13

Petitjean, P., Rauch, M., & Carswell, R. F. 1994, A&A, 291, 29

Petitjean, P., Riediger, R., & Rauch, M. 1996, A&A, 307, 417

Proga, D., Stone, J. M., & Kallman, T. R. 2000, ApJ, 543, 686

Reynolds, C. S. 1997, MNRAS, 286, 513

Romano, D., Silva, L., Matteucci, F., & Danese, L. 2002, MNRAS, 334, 444

Schneider, D. P., et al. 2007, AJ, 134, 102

Shemmer, O., Netzer, H., Maiolino, R., Oliva, E., Croom, S., Corbett, E., & di Fabrizio, L. 2004, ApJ, 614, 547

Shields, G. A. 1996, ApJ, 461, L9

Srianand, R., Petitjean, P., Ledoux, C., & Hazard, C. 2002, MNRAS, 336, 753

Steffen, A. T., Strateva, I., Brandt, W. N., Alexander, D. M., Koekemoer, A. M., Lehmer, B. D., Schneider, D. P., & Vignali, C. 2006, AJ, 131, 2826

Strateva, I. V., Brandt, W. N., Schneider, D. P., Vanden Berk, D. G., & Vignali, C. 2005, AJ, 130, 387

Tananbaum, H., et al. 1979, ApJ, 234, L9

Telfer, R. C., Kriss, G. A., Zheng, W., & Davidsen, A. 1998, ApJ, 509, 132

Tripp, T. M., Lu, L., & Savage, B. D. 1996, ApJS, 102, 239

Trump, J. R., et al. 2006, ApJS, 165, 1

Turnshek, D. A. 1986, in IAU Symp. 119, Quasars, ed. G. Swarup & V. K. Kapahi (Dordrecht: Reidel), 317

Vanden Berk, D. E., et al. 2001, AJ, 122, 549

Vignali, C., Brandt, W. N., & Schneider, D. P. 2003, AJ, 125, 433

Wampler, E. J., Chugai, N. N., & Petitjean, P. 1995, ApJ, 443, 586

Wise, J. H., Eracleous, M., Charlton, J. C., & Ganguly, R. 2004, ApJ, 613, 129

York, D. G., et al. 2000, AJ, 120, 1579

Yuan, Q., Green, R. F., Brotherton, M., Tripp, T. M., Kaiser, M. E., & Kriss, G. A. 2002, ApJ, 575, 687

Zhou, H., Wang, T., Wang, H., Wang, J., Yuan, W., & Lu, Y. 2006, ApJ, 639, 716